Title:

A Bayesian ground-motion model for volcano-tectonic earthquakes in southwest Iceland

Authors:

Victor M. Hernández-Aguirre[1]
Rajesh Rupakhety[1]

[1] Earthquake Engineering Research Centre, Faculty of Civil and Environmental Engineering, University of Iceland, Austurvegur 2a, 800 Selfoss, Iceland
Email: victorh@hi.is

Date of Preprint Posting:
4 June 2026

A Bayesian ground-motion model for volcano-tectonic earthquakes in southwest Iceland

Victor M. Hernández-Aguirre[a] · **Rajesh Rupakhety**[a]

Abstract

Volcano-tectonic earthquakes in Iceland and other volcanic regions produce ground motions that differ systematically from those of ordinary shallow crustal tectonic earthquakes. The recent unrest on the Reykjanes Peninsula has provided an exceptional opportunity to quantify these differences, with multiple intense swarms preceding and accompanying eruptive episodes. Building on Hernández-Aguirre et al. (2023; HR23), we develop an expanded empirical ground-motion model (GMM) for southwest Iceland using strong-motion recordings from 2021–2024. The dataset comprises >270 earthquakes ($M_w \geq 3.5$) and >4000 three-component records within $R_{epi} \leq 120$ km. We model PGA, PGV and 5%-damped pseudo-spectral acceleration over a broad period range for both horizontal and vertical components. The GMM is formulated as a Bayesian hierarchical mixed-effects regression with event and station random effects and calibrated using integrated nested Laplace approximation (INLA). Informative priors and a two-step calibration are used to reduce station–distance confounding under uneven station–distance coverage. The updated model confirms robust volcano-tectonic scaling characterized by elevated near-field amplitudes and rapid attenuation relative to tectonic models. Approximately 20% of records with $M_w \geq 4.2$ and $R_{epi} \leq 40$ km exhibit a PGA ratio V/H > 1, indicating that vertical seismic demand can be significant in near-source conditions. Compared with HR23, the total standard deviation is reduced, consistent with improved median predictions from added path/depth terms and site classification. The resulting model provides a statistically robust basis for PSHA and scenario-based risk assessment in Icelandic volcanic environments within the calibrated domain.

Keywords: Volcano-tectonic earthquakes, Reykjanes Peninsula, Ground-motion model, Vertical ground motion, Bayesian inference, Probabilistic seismic hazard assessment.

1. Introduction

The recent volcano-tectonic unrest of the Reykjanes Peninsula has exposed a persistent limitation in current ground-motion modelling for Iceland: conventional ground-motion models (GMMs) developed for ordinary tectonic crustal earthquakes do not necessarily represent the seismic shaking generated during volcanic-related events. This distinction is not only of seismological interest. In southwest Iceland, where volcanic systems, towns, geothermal facilities, and lifeline infrastructure coexist within a compact region, shallow volcano-tectonic (VT) earthquakes can contribute significantly to seismic risk even at moderate magnitude events.

Ground-motion modelling in volcanic regions has advanced significantly in recent years, particularly in densely instrumented areas such as Italy. Studies from Campi Flegrei, Mount Etna, and Ischia have shown that volcanic earthquakes can exhibit scaling characteristics that differ systematically from those of ordinary tectonic earthquakes, including very shallow source depths, relatively large near-field amplitudes, and rapid attenuation with distance (Lanzano & Luzi, 2020; Scala et al., 2026; Tusa et al., 2020; Tusa & Langer, 2016). These behaviours are commonly interpreted as reflecting the combined influence of magmatic and fluid-driven source processes, shallow crustal heterogeneity, and complex wave-propagation conditions in volcanic environments.

Despite their typically moderate magnitudes, VT earthquakes can generate shaking levels that are important for engineering applications, especially in near-source conditions, where observations can exceed those prescribed by building codes for seismic design (Iervolino et al., 2024). Recent studies have also highlighted the relevance of the vertical component of motion in volcanic settings, especially at short periods where vertical amplitudes may become comparable to horizontal amplitudes and influence structural demand in ways not represented adequately by conventional assumptions (Ramadan et al., 2023). At the same time, volcanic environments are highly diverse, ranging from stratovolcanoes to caldera systems, and ground-motion characteristics can vary substantially depending on regional geology, source mechanisms, and shallow crustal structure. Consequently, the transferability of volcanic-region GMMs between different tectonic and volcanic settings remains limited, motivating the development of regionally calibrated models tailored to the physical and statistical characteristics of local volcanic seismicity.

The 2021 Geldingadalir and 2022 Meradalir eruptions at Fagradalsfjall in the Reykjanes Peninsula were preceded by intense swarms of volcano-tectonic earthquakes. These swarms produced some of the strongest ground accelerations recorded in Iceland since the 2008 Mw 6.3 Ölfus earthquake. Hernández-Aguirre et al. (2023), hereafter HR23, analyzed the strong-motion records from the 2021 and 2022 Fagradalsfjall swarms and identified several features with direct r engineering relevance. First, near-source peak ground accelerations (PGAs) were higher than Icelandic tectonic models. Second, the waveforms contained a distinct combination of impulsive high-frequency arrivals and unusually rich long-period content. Third, response spectra showed broad plateaus and elevated spectral ordinates at periods that atypical for earthquakes of M_w 5–5.7. Finally, attenuation was faster than that inferred for tectonic Icelandic earthquakes, while the magnitude scaling was weaker than in volcanic ground-motion models developed for Italy (Lanzano & Luzi, 2020).

These observations have direct implications for seismic hazard assessment in southwest Iceland, where hazard may be strongly influenced by episodes of volcanic unrest rather than by the long-term tectonic background alone. Because critical energy-related infrastructure in Iceland is often located within or adjacent to active systems, models that do not account for the distinct source-path characteristics of volcano-tectonic earthquakes may bias both probabilistic seismic hazard assessment (PSHA) and scenario-based estimates of ground shaking, particularly at short distances where the differences from tectonic scaling are the strongest.

HR23 provided the first Iceland-specific GMM for volcano-tectonic earthquakes. The model was calibrated for the geometric mean of the horizontal (GMH) components of PGA, peak ground velocity (PGV), and 5%-damped pseudo-spectral acceleration (PSA) using records from the early Fagradalsfjall swarms. It represented an important first step, but was intentionally limited in scope. The calibration relied on a relatively small number of high-quality records, focused on rock-site conditions, excluded stations with suspected strong site effects, and did not include a separate model for the vertical component. These choices were appropriate given the limited data available at the time and the objective of isolating source-path scaling in a relatively controlled dataset. However, they also limited the model's applicability for operational hazard calculations, which require predictions across a broader set of stations, site conditions, and intensity measures (IMs).

Since HR23, continued unrest on the Reykjanes Peninsula has substantially expanded the available strong-motion database. Continued seismic activity and repeated eruptive episodes have produced a significantly larger dataset of recordings from small-to-moderate volcano-tectonic earthquakes. This expanded dataset makes it possible to revisit the modelling problem with a broader scope. In particular, the new data allow the inclusion of additional events and stations, geology-based site classes, a broader magnitude range, and vertical spectral ordinates. These additions are essential for a model to be suitable for engineering and hazard-assessment applications.

The present paper develops an updated ground-motion model for shallow volcano-tectonic earthquakes in southwest Iceland. The model, referred to here as HR26, extends HR23 in three principal ways. First, it uses an expanded dataset comprising 4238 records from 273 earthquakes with $M_w \geq 3.5$ recorded within an epicentral distance of 120 km. Second, it includes a geology-based site classification with four site classes, allowing first-order site amplification to be represented explicitly rather than absorbed into station residuals or median source-path terms. Third, it develops separate models for the geometric mean and RotInv (Rotational-Invariant median; Rupakhety & Sigbjörnsson, 2013) of the horizontal components, as well as the vertical component, thereby enabling applications involving vertical seismic demand and vertical-to-horizontal spectral ratios.

A further difference from HR23 is methodological. Whereas the previous model was developed using a mixed-effects regression framework, the present study formulates the GMM as a partially non-ergodic Bayesian hierarchical model calibrated using integrated nested Laplace approximations (INLA) (Rue et al., 2009). This framework is particularly well suited to the present database because observations are unevenly distributed across events and stations, some model coefficients exhibit trade-offs, and prior information from HR23 can be used to regularize weakly constrained parameters. INLA enables efficient Bayesian inference for period-by-period GMM calibration without the computational burden associated with full Markov chain Monte Carlo sampling.

The paper is organized as follows. Section 2 summarizes the regional tectonic and volcanic setting of the Reykjanes Peninsula and describes the expanded strong-motion database. Section 3 describes the site classification. Section 4 describes the Bayesian hierarchical model formulation, including the median function, random effects, prior specification, and INLA implementation. Section 5 presents the model coefficients and spectral trends for the horizontal and vertical components, compares the proposed model with HR23 and selected tectonic and volcanic GMMs, and discusses residual decomposition and variability. Finally, Section 6 discusses implications of the results and summarizes the main conclusions and limitations.

2. Regional setting and strong-motion database

2.1 Reykjanes Peninsula volcanic and tectonic setting

The Reykjanes Peninsula is the onshore continuation of the Reykjanes Ridge and forms an oblique transition between the offshore Mid-Atlantic plate boundary, the Western Volcanic Zone, and the South Iceland Seismic Zone (Einarsson, 1991). The plate boundary follows an approximately ENE–WSW trend along the peninsula, whereas the relative motion between the North American and Eurasian plates is oblique to this trend (Björnsson et al., 2020). As a result, deformation is accommodated by a combination of volcanism, normal faulting, fissure opening, dyke intrusion, and strike-slip faulting. The peninsula contains several volcanic systems, including Reykjanes, Svartsengi, Fagradalsfjall, Krýsuvík, Brennisteinsfjöll, and Hengill (Sæmundsson et al., 2020).

The present unrest began in late 2019, after a long period without eruptions on the peninsula. Since then, inflation episodes, intense earthquake swarms, dyke intrusions, and repeated eruptions have since occurred across the region. The 2021 Geldingadalir and the 2022 Meradalir eruptions were preceded by intense seismic swarms in the Fagradalsfjall volcanic system. HR23 described the early stage of this unrest and showed that the February–March 2021 swarm included several earthquakes with magnitude $M \geq 5$, the largest being the 24 February 2021 M_w 5.6 event. Unrest has since migrated among several volcanic systems and continues to the present day. The latest eruptions have occurred in the vicinity of the Sundhnúkur crater row (Sundhnjúkagígur, see Figure 1), close to the town of Grindavík.

The seismicity during these swarms reflects the complex volcanic-tectonic character of the region. Many of the larger events have strike-slip mechanisms broadly compatible with the regional transform component of deformation, but their occurrence is temporally and spatially linked to magmatic intrusion and dyke propagation (Fischer et al., 2026). This hybrid context is relevant for ground-motion modelling. Volcanic seismicity can range from high-frequency volcano-tectonic (VT) earthquakes caused by brittle failure, to long-period (LP) events associated with fluid processes, and hybrid events combining features of both. The strong-motion records analysed by HR23 showed clear P- and S-wave arrivals and high-frequency onsets, but also substantial low-frequency energy. For engineering purposes, these records are best regarded as shallow volcano-tectonic earthquakes, rather than ordinary tectonic earthquakes.

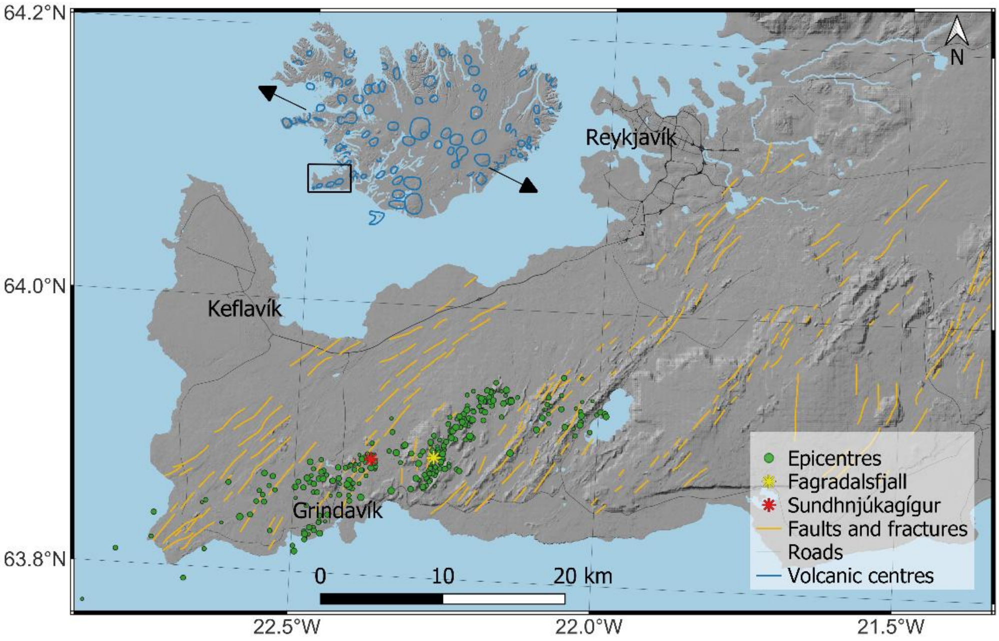

Figure 1. The Reykjanes Peninsula. The asterisks indicate the location of the Fagradalsfjall and Sundhnjúkagígar eruption zones. The dots show the epicentres of earthquakes considered in this study. Faults, fractures and volcanic centres are from Jóhannesson & Sæmundsson (2009). The inset shows the location of the peninsula (black square) and the spreading direction between the North American and Eurasian tectonic plates, indicated by black arrows.

2.2 Magnitude estimates

A key requirement for developing a stable GMM is a consistent magnitude scale. The catalogue of the Icelandic Meteorological Office (IMO, 2025) provides automatically computed and manually reviewed earthquake locations and magnitude estimates based on the South Iceland Lowland seismic network. This system was designed primarily for robust monitoring of Icelandic seismicity, including small earthquakes. However, local magnitude estimates can underestimate larger events because they rely on high-pass filtered velocity amplitudes from short-period seismometers (Jónasson et al., 2021). This effect was discussed by HR23.

To independently assess earthquake size and source properties, moment tensor inversions were performed for selected events (Birgisdóttir, 2025) using ISOLA (Sokos & Zahradnik, 2008). The inversion workflow consists of event definition, waveform preparation, computation of Green's functions, and waveform inversion. For each event, the initial hypocentral location, origin time, depth, and magnitude were taken from the IMO catalogue. The seismograms were processed consistently through alignment, resampling, tapering and filtering. Green's functions were computed using the frequency-wavenumber method (Bouchon, 1981) and a common one-dimensional crustal velocity model. A deviatoric moment tensor inversion was then performed using a single point source following the Kikuchi and Kanamori method (Kikuchi & Kanamori, 1991). Source depth was allowed to vary in discrete steps around the catalogue value.

For each trial depth, ISOLA provides waveform correlation, seismic moment, moment magnitude (hereafter denoted as M_{INV}), variance reduction, and the corresponding fault-plane solution. The preferred solution was selected as that providing the largest variance reduction. As shown in Figure 2, the resulting magnitudes are generally consistent with those reported by the Euro-Mediterranean Seismological Centre (EMSC) (Bossu et al., 2024). In contrast, the bias of the IMO magnitude estimates at larger magnitudes is evident. Consequently, EMSC moment magnitudes are adopted for regression. This choice provides a consistent M_w scale and reduces the likelihood that magnitude-dependent trends in the GMM are biased by local magnitude saturation or underestimation.

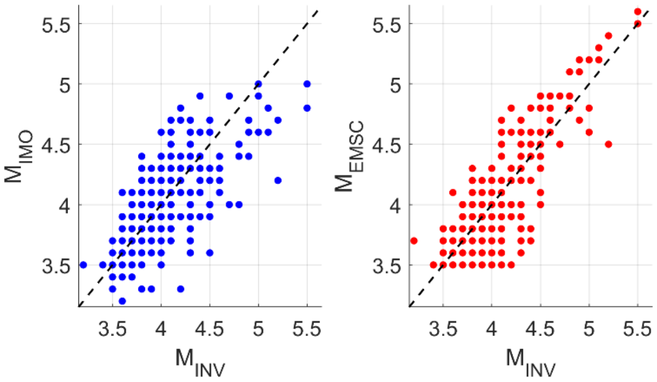

Figure 2. Comparison of magnitude estimates from IMO (IMO, 2025) and EMSC (Bossu et al., 2024) against moment magnitudes obtained from ISOLA waveform inversion (M_{INV}) (Sokos & Zahradnik, 2008).

Magnitude uncertainty is not explicitly propagated in the current model. This is a limitation, particularly for smaller events. Nevertheless, the Bayesian formulation partly mitigates the effects of magnitude uncertainty through coefficient regularization and the inclusion of event random effects. Future work could explicitly account for magnitude uncertainty by treating moment magnitude as a latent variable within an errors-in-variables framework (Strasser et al., 2009), thereby reducing bias in magnitude scaling and improving the interpretation of residual variability.

2.3 Expanded strong-motion dataset

The database used in this study was assembled from the Icelandic Strong Motion Network, IceSMN (Rupakhety & Ólafsson, 2015), operated by the Earthquake Engineering Research Centre of the University of Iceland. IceSMN provides three-component acceleration recordings at stations distributed across the Reykjanes Peninsula, the Reykjavík region, South Iceland, and other seismically active parts of the country. The present dataset includes volcano-tectonic earthquakes associated with the Reykjanes unrest, recorded between 2021 and 2024. Locations of the epicentres, taken directly from IMO, are shown in Figure 1. The final regression database consists of 4238 records from 273 earthquakes with EMSC $M_w \geq 3.5$ and epicentral distance $R_{epi} \leq 120$ km. Figure 3 shows the scatter of event M_w versus R_{epi} for all records in the dataset used in the study.

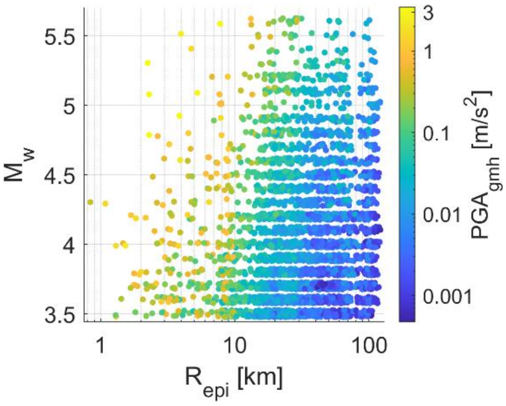

Figure 3. Magnitude–distance distribution of the dataset. A small vertical jitter was added to reduce overlap. Marker colour indicates recorded horizontal PGA (geometric mean).

The event-station distribution is unbalanced; some larger events are recorded by many stations over a broad distance range, whereas smaller events are recorded mainly at nearby stations. Similarly, some stations contribute many records because they are close to the active volcanic systems, whereas more distant stations contribute fewer observations. This unbalanced sampling is one of the reasons for using a hierarchical mixed-effects framework, as discussed later.

For each record, the two horizontal acceleration components and the vertical component were processed consistently. Records affected by clipping, timing problems, anomalous baselines, or insufficient signal-to-noise ratio are excluded. Instrument correction, baseline correction, filtering, and IM calculation are carried out using a uniform workflow. The primary horizontal IM is the geometric mean of the two as-recorded horizontal components. This choice follows Lanzano & Luzi (2020) and HR23 and allows continuity with the earlier model. For completeness, we also include the median RotInv IM (Rupakhety & Sigbjörnsson, 2013), which has been shown to similar to RotD50.

The IMs considered in the model are PGA, PGV and 5%-damped PSA(T). The oscillator periods span the short-period range relevant for low-rise buildings and non-structural components, as well as intermediate and long periods. The same period vector is used for the horizontal and vertical models to facilitate comparison of spectral coefficients and vertical-to-horizontal ratios. Period smoothing of coefficients is discussed as a future refinement, but is not imposed in the present version to avoid masking period-specific features of the volcanic records.

The vertical component is modelled separately. This extension is important for several reasons. First, HR23 observed that vertical PGAs were often comparable to horizontal PGAs for nearby stations, although vertical velocities were generally lower, indicating richer high-frequency content in the vertical component. Second, vertical ground motion can be relevant for the seismic assessment of short-span bridges, precast elements, non-structural components, industrial equipment, geothermal and hydropower infrastructure, and facilities located close to shallow sources. Third, vertical-to-horizontal spectral ratios may differ in volcanic environments because of shallow source depths, high-frequency radiation, near-source wavefield effects, and site response. This approach allows the vertical model to have its own magnitude scaling, attenuation, site terms, and variability components, rather than imposing proportionality to the horizontal model.

3. Site classification

Site effects are a major source of ground-motion variability in Iceland. The near-surface geology of the Reykjanes Peninsula and South Iceland is complex, reflecting volcanic activity, glacial processes, marine transgression and regression, lava emplacement, hyaloclastite formation, tephra deposition, and sediment accumulation (Sæmundsson, 1979). In many areas, sedimentary layers have been covered by layers of basaltic lava and hyaloclastite breccia post-glacial age, creating geological structures with thin layers of lava rock on top of, or embedded in, unconsolidated sediments (Olafsdottir et al., 2023). In other locations, weathered volcanic materials, tephra, fractured lava, and shallow sedimentary pockets may produce site amplification that cannot be captured adequately by a single proxy.

The most common site proxy in GMMs is $V_{S,30}$. However, $V_{S,30}$ is not available for many Icelandic strong-motion stations and may not fully capture the specific soil-rock structures found in Icelandic volcanic environments. For example, a site with a shallow lava cap over softer material may have a relatively high near-surface shear-wave velocity but still exhibit strong impedance contrasts and frequency-dependent amplification. Conversely, stations located on mapped lava or rock units may have different responses because of weathering, fractures, topography, or shallow sediment lenses.

HR23 avoided this complication by calibrating the model for rock-site conditions and excluding stations suspected of strong site effects, such as Krýsuvík. That approach helped isolate source-path scaling, but it limited the model's applicability. The expanded dataset includes a broader range of stations and site conditions, making it necessary to introduce an explicit site predictor. In this study, site effects are represented using a geology-based classification with four classes (Figure 4), following the approach of recent Icelandic site-amplification studies (Darzi et al., 2024). The classes are intended to represent, in broad terms, hard rock (A), soft rock (B), lava with interbedded sediments (C), and thick soil deposits (D). These were developed by cross-referencing geological maps with PGA site-to-site residuals (δ_{S2S}) obtained from the IceSMN dataset with respect to a local GMM (Kowsari et al., 2020).

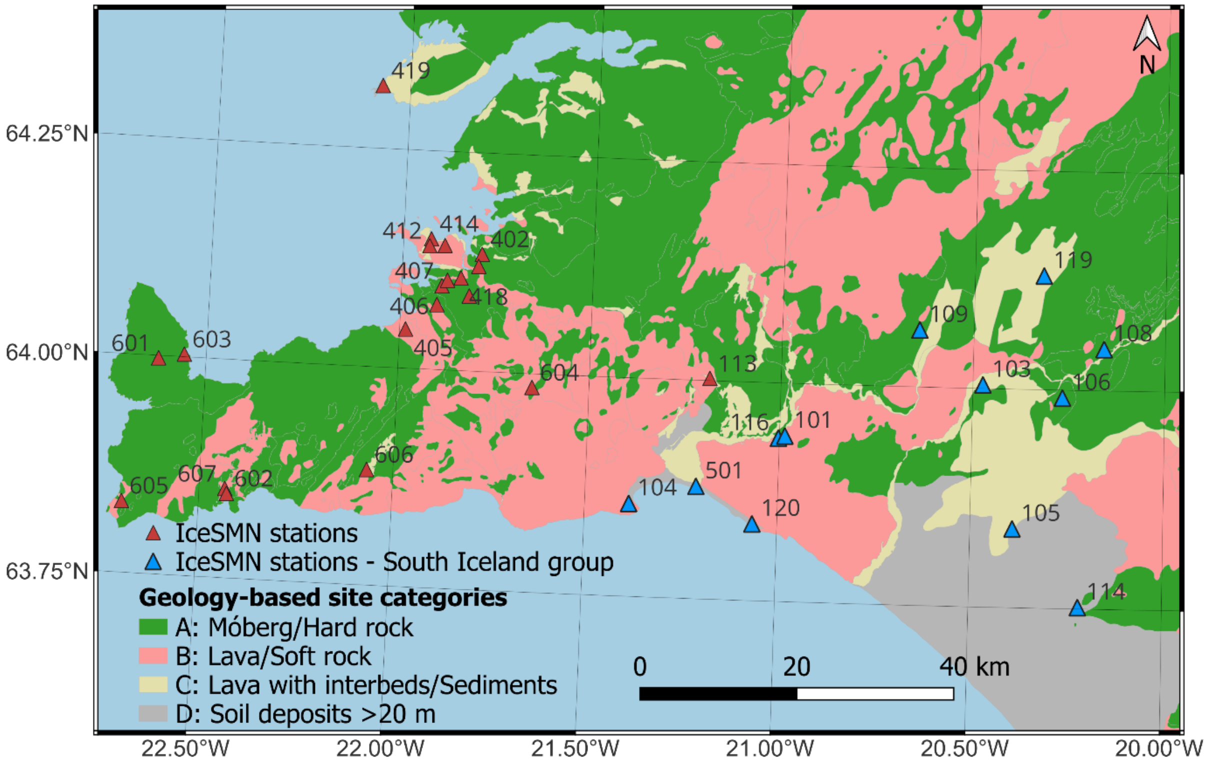

Figure 4. Geology-based site classes for southwest Iceland. The triangles are the locations of the accelerometers of the IceSMN (Rupakhety & Ólafsson, 2015). Blue stations correspond to the South Iceland lowland path group.

This classification is necessarily approximate. It should not be interpreted as a substitute for site-specific geotechnical characterization or as a direct equivalent of Eurocode 8 $V_{S,30}$-based classes. Instead, it is an operational predictor designed to separate first-order amplification trends from source and path terms. A station-specific random effect is retained in the model to capture persistent deviations not explained by the site class. This is important because broad geological categories cannot account for local topography, shallow layering, lava-sediment impedance contrasts, or installation-specific effects.

4. Bayesian hierarchical ground-motion model

4.1 Bayesian inference

The proposed ground-motion model is formulated as a Bayesian hierarchical mixed-effects regression, consistent with the framework commonly adopted in empirical ground-motion modelling (e.g., Stafford, 2014). Let $y_{es} = \log_{10} Y_{es}$ denote the logarithmic IM for event e and station s. The model can be written as:

$$y_{es} = \mu_{es}(\boldsymbol{\beta}) + \delta \mathrm{B}_e + \delta \mathrm{S}_s + \delta \mathrm{W}_{0,es}, \tag{1}$$

where $\mu_{es}(\boldsymbol{\beta})$ is the deterministic median prediction defined by the fixed-effect coefficients $\boldsymbol{\beta}$. The station term $\delta \mathrm{S}_s$ and the within-event residual $\delta \mathrm{W}_{0,es}$ are assumed to follow zero-mean Gaussian distributions (Strasser et al., 2009):

$$\delta S_s \sim \mathcal{N}(0, \phi_S^2), \delta \mathrm{W}_{0,es} \sim \mathcal{N}(0, \sigma_0^2),$$

where ϕ_S is the site-to-site standard deviation, σ_0 is the remaining within-event standard deviation.

To account for magnitude-dependent between-event variability, the between-event term is modelled as heteroskedastic. Specifically, we express the event effect as a weighted combination of two independent event components:

$$\delta B_e(M_w) = w(M_w)\, \delta B_e^{(1)} + [1 - w(M_w)] \delta B_e^{(2)}, \tag{2}$$

with

$$\delta B_e^{(1)} \sim \mathcal{N}(0, \tau_1^2), \delta B_e^{(2)} \sim \mathcal{N}(0, \tau_2^2).$$

Here M_w is the event magnitude, and the weight $w(M_w) \in [0,1]$ is prescribed to decrease linearly from 1 at $M_w = 3.5$ to 0 at $M_w = 4.5$, and remain constant outside this range. In practice, this is implemented as two independent between-event terms with distinct variances, combined using the deterministic magnitude-dependent weight $w(M_w)$. This construction yields the following effective standard deviation for the between-event random effect:

$$\tau_{\mathrm{eff}}(M) = \sqrt{w(M)^2 \tau_1^2 + (1 - w(M))^2 \tau_2^2}. \tag{3}$$

Under this formulation, the likelihood remains Gaussian:

$$y_{es} \mid \boldsymbol{\beta}, \delta B_e^{(1)}, \delta B_e^{(2)}, \delta S_s \sim \mathcal{N}(\mu_{es}(\boldsymbol{\beta}) + \delta B_e(M_w) + \delta S_s, \sigma_0^2). \tag{4}$$

In a Bayesian setting, inference is based on the posterior distribution:

$$p(\boldsymbol{\theta}, \mathbf{b} \mid \mathbf{y}) \propto p(\mathbf{y} \mid \boldsymbol{\theta}, \mathbf{b})\, p(\mathbf{b} \mid \boldsymbol{\theta})\, p(\boldsymbol{\theta}), \tag{5}$$

where $\mathbf{b}$ denotes the collection of latent event and station random effects, i.e., $B_e^{(1)}, \delta B_e^{(2)}, \delta S_s$, $\boldsymbol{\theta} = (\boldsymbol{\beta}, \tau_1, \tau_2, \phi_S, \sigma_0)$ is the fixed effects and variance components, $p(\boldsymbol{\theta})$ the prior density of the parameters, and $p(\mathbf{y} \mid \boldsymbol{\theta}, \mathbf{b})$ the likelihood function. This formulation corresponds to a latent Gaussian model (Rue et al., 2009).

The use of a Bayesian framework is particularly advantageous for the present dataset, which is heterogeneous and spatially unbalanced. It is clear from Figure 1 and Figure 4 that any given station has epicentral distances in a limited range. As in many regional GMMs, trade-offs may arise between distance attenuation, site effects, and path corrections due to non-uniform station coverage (Kowsari et al., 2020). For example, near-source stations may be concentrated in specific geological environments, leading to partial confounding between attenuation and site amplification. Similarly, site-class coefficients may trade off with station-specific effects when some classes are sparsely sampled. These issues are well known in mixed-effects regression and can lead to unstable or poorly constrained coefficients in sparse datasets.

An additional advantage of the Bayesian framework is that it provides a direct quantification of epistemic uncertainty through the posterior distributions of the model coefficients and hyperparameters. This uncertainty can be propagated into hazard calculations, for example through logic-tree implementations.

4.2 Median functional form

For a given event e and station s, the fixed-effect part of the model (in base-10 logarithmic units) is written as:

$$\mu_{es}(\boldsymbol{\beta}) = \mathrm{a} + \Delta a I_{e,deep} + \mathrm{f_M}(\mathrm{M_w}) + \mathrm{f_D}\left(\mathrm{R}_{\mathrm{epi},es}, \mathrm{M_w}, I_s\right) + \mathrm{f}_{\mathrm{site},s}, \tag{6}$$

where a is the intercept, $I_{e,deep}$ is an indicator variable equal to one for events deeper than 5 km and zero otherwise, $R_{\mathrm{epi},es}$ is the epicentral distance (km), $f_{\mathrm{site},s}$ is the site term and I_s is a station/path-group indicator equal to one for stations whose records predominantly sample propagation from Reykjanes toward the South Iceland Lowland (blue markers in Figure 4), and zero otherwise. Epicentral distance is used as the distance metric because it is available consistently for all events and is more common than hypocentral distance in routine seismic hazard assessment.

The magnitude scaling is represented by a bilinear function:

$$f_M(\mathrm{M_w}) = \begin{cases} b_1(\mathrm{M_w} - M_h), & \mathrm{M_w} \le M_h \\ b_2(\mathrm{M_w} - M_h), & \mathrm{M_w} > M_h \end{cases}, \tag{7}$$

where M_h is the hinge magnitude, fixed at $M_h = 5$, based on exploratory analysis indicating a change in scaling behaviour around this value for some periods.

The distance scaling is represented by the function:

$$f_D\left(R_{epi}, M_w, I_s\right) = \left[c_1 + \Delta c_1 I_s + c_2 M_{\text{pos}}\right]\log_{10}\left(\sqrt{R_{\text{epi},es}^2 + h_{eff}^2}\right). \tag{8}$$

Here $M_{\text{pos}} = \max\left(M_w - M_h, 0\right)$, so that c_2 contributes only when $M_w > M_h$ and has no effect for $M_w \le M_h$. This term was introduced to reduce bias at large magnitudes observed in initial tests. The coefficient Δc_1 allows the effective distance scaling to differ for these paths relative to paths within the Reykjanes Peninsula and toward Reykjavík, capturing systematic path-dependent attenuation differences not represented by the baseline term c_1. h_{eff} is a pseudo-depth parameter that serves to regularize the distance metric at short distances and mimic finite-source saturation effects, defined as

$$h_{eff} = h_1 + 0.25 \cdot \left[max(M_w - 3.5,\ 0)\right]^2,$$

where h_1 (km) is obtained from the regression and the second term is introduced to represent the increase in finite-source saturation with magnitude.

The site term is defined using a categorical formulation:

$$f_{\text{site,s}} = \begin{cases} 0, & \text{site class A,} \\ s_B, & \text{site class B,} \\ s_C, & \text{site class C,} \\ s_D, & \text{site class D.} \end{cases} \tag{10}$$

Nonlinear site response was not explicitly modelled because the site information is limited to broad geological classes and the dataset provides limited constraint on amplitude-dependent amplification. The site terms should therefore be interpreted as average linear amplification over the range of observed shaking intensities.

4.3 Model calibration

In principle, the posterior distribution in eq. (5) could be explored using Markov chain Monte Carlo (MCMC) methods, which are widely used in non-ergodic and fully Bayesian GMM developments (Arroyo & Ordaz, 2010; Kowsari et al., 2020; Kuehn & Scherbaum, 2015; Lavrentiadis et al., 2023). However, making full MCMC sampling is computationally costly.

Inference in this study is instead performed using the integrated nested Laplace approximation (INLA) (Kuehn, 2021; Rue et al., 2009), which provides fast deterministic approximations to marginal posterior distributions in latent Gaussian models (LGMs). In an LGM, the linear predictor is expressed as an additive function of a Gaussian latent field and a set of hyperparameters, and INLA exploits the resulting conditional independence structure to approximate the posterior marginal distributions $p(\boldsymbol{\theta}, \mathbf{b} \mid \mathbf{y})$ via nested Laplace approximations and numerical integration over $\boldsymbol{\theta}$. In the present model, the latent field includes the event and station effects (and associated variance components), while the likelihood is Gaussian on the $\log_{10}$IM scale. We use INLABRU (Bachl et al., 2019) as a convenient interface to specify the model—including the distance predictor that depends on the effective depth h_{eff}— and to fit the resulting LGM with INLA, avoiding full MCMC sampling while retaining accurate marginal posterior summaries for coefficients and variance components.

To mitigate confounding between near-field station effects and distance scaling, we adopt a two-step calibration coupled with informative or weakly informative priors on selected coefficients (Kowsari et al., 2020; Stafford, 2014). In preliminary fits, the station random effects became inflated for the subset of stations that dominate the short-distance range, indicating that part of the residual distance trend was being absorbed by station intercepts and biasing the near-field median scaling.

Stage 1 fits the median model without station random effects. For the first period (PGA), we assign Gaussian priors with the mean (μ) and standard deviation (SD) listed in Table 1. The priors for b_1, c_1, and h_1 are centred on the HR23 model, while the site-class coefficients are given priors consistent with increasing average amplification from class A to class D. Standard deviations are chosen to be sufficiently broad that the likelihood dominates where the data are informative.

For subsequent oscillator periods i, we promote smooth period-to-period behaviour by defining priors centred on the previous period's posterior mean, $\mu_i = \hat{\mu}_{i-1}$, with inflated prior standard deviations to avoid over-constraining spectral variability (Table 2). This regularization reduces spurious period-to-period fluctuations driven by weak identification rather than by physical differences.

Table 1. Priors used for fitting PGA in Step-1.

Coeff	a	Δa	b_1	b_2	c_1	c_2	Δc_1	s_B	s_C	s_D	h_1
μ	1	0	0.5	0.3	-2	0.3	0.3	0.05	0.1	0.2	5
SD	3	0.1	0.1	0.1	0.2	0.1	0.2	0.1	0.1	0.1	0.2

Table 2. Priors used for fitting period *i* in Step-1.

Coeff	a_i	Δa_i	$b_{1,i}$	$b_{2,i}$	$c_{1,i}$	$c_{2,i}$	$\Delta c_{1,i}$	$s_{B,i}$	$s_{C,i}$	$s_{D,i}$	$h_{1,i}$
μ	1	$\widehat{\Delta a}_{i-1}$	$\hat{b}_{1,i-1}$	$\hat{b}_{2,i-1}$	$\hat{c}_{1,i-1}$	$\hat{c}_{2,i-1}$	$\widehat{\Delta c}_{1,i-1}$	$\hat{s}_{B,i-1}$	$\hat{s}_{C,i-1}$	$\hat{s}_{D,i-1}$	$\hat{h}_{1,i-1}$
SD	3	0.1	0.05	0.1	0.1	0.1	0.1	0.05	0.05	0.05	0.3

Random-effects standard deviations are assigned penalized-complexity (PC) priors (Simpson et al., 2017), which favour the base model (smaller random-effect variance) unless supported by the data. PC priors are specified by (U, α) such that $P(\sigma > U) = \alpha$, where σ is the random-effect standard deviation. We use $U_{\tau_1} = 0.15, U_{\tau_2} = 0.1, U_{\phi_S} = 0.03, U_{\sigma_0} = 0.25$, with $\alpha_{\tau_1} = \alpha_{\tau_2} = \alpha_{\sigma_0} = 0.05 \; and \; \alpha_{\phi_S} = 0.001$. The restrictive prior on ϕ_S is used to limit the tendency of station effects to absorb residual distance trends under the uneven station–distance coverage described above.

Step 2 introduces station terms while anchoring fixed-effect priors to Step-1 posteriors to prevent station terms from re-shaping attenuation. This stabilizes the partitioning of variability into τ_1, τ_2, ϕ_S, and σ_0, and improves interpretability of the resulting model.

PGV models are calibrated using the same two-step procedure, with priors based on HR23. For the vertical component, we follow the same calibration strategy as for the horizontal models, but in Step 1 for PGA we assign priors centred on the posterior means from the horizontal model.

5. Model results

5.1 Horizontal ground-motion

5.1.1 Model coefficients and median scaling

The following discussion focuses on the GMH component. The posterior median fixed-effect coefficients for the GMH IMs are summarized in Table A1 in Appendix1. For completeness, the corresponding posterior median coefficients for RotInv are provided in Table A2. Although the updated coefficients differ from those of the earlier HR23 model, a direct coefficient-by-coefficient comparison is not meaningful because the functional form has been modified. Consequently, the comparisons are more appropriately made in terms of the resulting median predictions, attenuation trends, and residual structure.

Figure 5 shows the posterior marginal distributions of the model coefficients for GMH PGA. The posterior distributions are generally unimodal and approximately Gaussian. The main exceptions are the variance-component standard deviations, which show mild positive skewness, as expected for scale parameters constrained to be positive.

A useful indication of parameter resolution is provided by the the ratio of the posterior mean to the posterior standard deviation (Kowsari et al., 2020). Although these ratios are not shown for brevity, most fixed-effect coefficients have posterior mean that are more than approximately two posterior standard deviations, suggesting that the corresponding effects are reasonably well constrained by the data. This measure is used here as an indication of parameter resolution rather than a formal significance test.

Further insight into parameter identifiability is provided by the posterior Pearson cross-correlation matrix, shown in Figure 6 for GMH PGA. For compactness, only the PGA matrix is shown, but similar patterns are observed for PSA ordinates. These matrices reveal dependencies among model parameters that are often assumed independent in conventional GMM formulations. Correlation values close to ± 1 indicate strong posterior dependence and potential trade-offs between parameters. In the present model, most parameter correlations are relatively weak, suggesting limited confounding between model terms. A moderate correlation is observed between the station-to-station variability term, ϕ_S, and the distance-attenuation terms, $c_1$and Δc_1. This behaviour is consistent with the near-field station/path confounding identified in preliminary model development. The adopted two-step calibration reduces, but does not eliminate, this dependency. Overall, Figure 5 and Figure 6 indicate that the horizontal model calibration is stable and that the principal model coefficients are reasonably well constrained by the data.

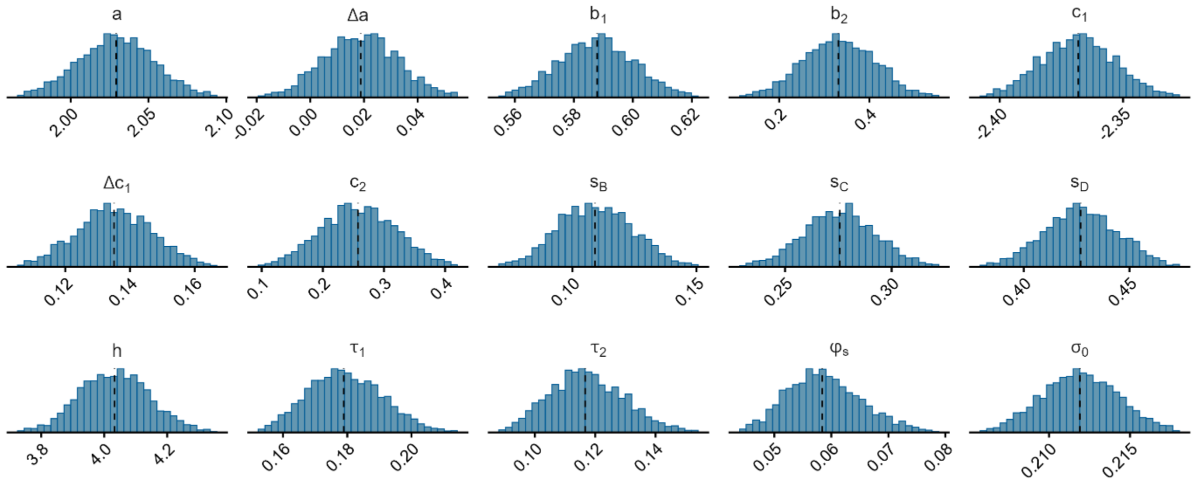

Figure 5. Posterior distributions of GMH PGA model parameters. The dashed lines show the median values.

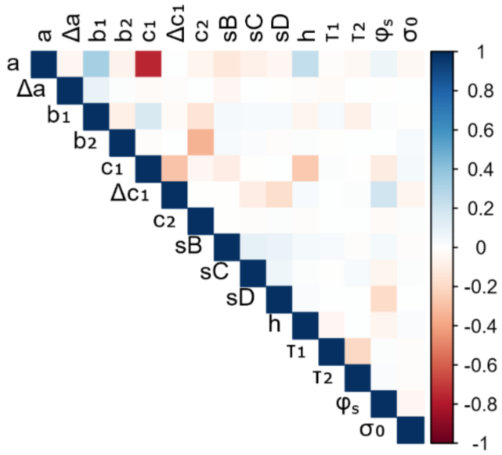

Figure 6. Pearson's cross-correlation coefficient matrix from GMH PGA posterior model parameters.

The distance-attenuation coefficient remains large and negative, confirming the rapid attenuation of ground motions with distance for VT earthquakes, as previously discussed in HR23, and seen in other volcanic regions (Ramadan et al., 2023; Scala et al., 2026). The attenuation correction term for paths crossing the South Iceland lowland, Δc_1, is positive. Since the effective attenuation coefficient for this path group is $c_1 + \Delta c_1$, a positive Δc_1 indicates lower apparent attenuation with distance. This behaviour is consistent to differences in crustal structure between the two regions. The Reykjanes Peninsula has experienced repeated recent intrusive episodes, promoting fracture development (Ducrocq et al., 2024), potentially increasing scattering and attenuation, whereas the South Iceland lowland is comparatively less fractured and may allow more efficient seismic-wave propagation.

The introduction of a hinge magnitude indicates that magnitude scaling above $M_w 5$ is generally weaker than below $M_w 5$. However, the larger-magnitude part of the model is necessarily less constrained because the number of events above $M_w 5$ is limited. This is reflected in Figure 5, where the posterior distribution of b_2 is wider than that of b_1. Consequently, the weaker scaling above $M_w 5$ should be interpreted as the trend supported by the available dataset, while recognizing that additional large-magnitude observations would be required to further constrain this behaviour.

At short periods, the site coefficients show a physically reasonable increase from site class A to site class D. The persistence of positive site-class coefficients after including station random effects suggests that the geological classification captures a regional site-response trend rather than merely absorbing the behaviour of a few anomalous stations. Interestingly, at intermediate-to-long periods the coefficients for classes B and C are close zero, indicating no consistent amplification with respect to class A. In logarithmic units, the coefficient for class D corresponds to substantial median amplification relative to class A. Overall, the largest differences in amplification between classes is obtained at high frequencies, in accordance consistent with previous studies (Rahpeyma et al., 2023). Nevertheless, the station-to-station variability remains non-negligible, indicating that broad geological classes alone do not fully capture local site effects.

The correction term for deep events, Δa, becomes increasingly relevant at intermediate-to-long periods. The negative coefficient indicates systematically lower long-period amplitudes for deeper events relative to shallower events even after accounting for magnitude, distance, and site effects. This behaviour is consistent with the findings of Tusa and Langer (2016) for ground motions at Mount Etna, Italy. They reported that shallow events exhibit characteristics similar to LP earthquakes, including enhanced low-frequency content, whereas deeper events more closely resemble VT earthquakes and show spectral characteristic more typical of tectonic earthquakes in active crustal regions. The physical mechanisms controlling these depth-dependent spectral differences remain uncertain and warrant further investigation.

Figure 7 compares observed GMH PGA values and PSA ordinates at $T = 1$ s recorded by the IceSMN network with the proposed median GMM for site class B. Predictions from HR23, the Italian volcanic GMM RLS23 (Ramadan et al., 2023), and the Icelandic tectonic GMM KS20 (Kowsari et al., 2020) are also shown for reference. For $R_{epi} \geq 45$km, the proposed model includes the additional path correction Δc_1 since data points from this distance range are from the South Iceland lowland group. The proposed model is broadly consistent with the observed ground motions. Compared with HR23, the updated model predicts similar overall trends but slightly larger near-source amplitudes. This difference is consistent with the expanded dataset and the revised functional form, which better captures the near-source observations from recent Reykjanes seismicity. The RLS23 model gives relatively similar predictions within the magnitude range where it is well constrained, approximately $M_w < 4.6$, but larger differences emerge outside this range. In contrast, the KS20 model exhibits slower attenuation with distance and lower near-source amplitudes, making it less consistent with the volcanic dataset. This agrees with the conclusion of HR23 that volcano-tectonic ground motions differ systematically from those associated with ordinary tectonic events.

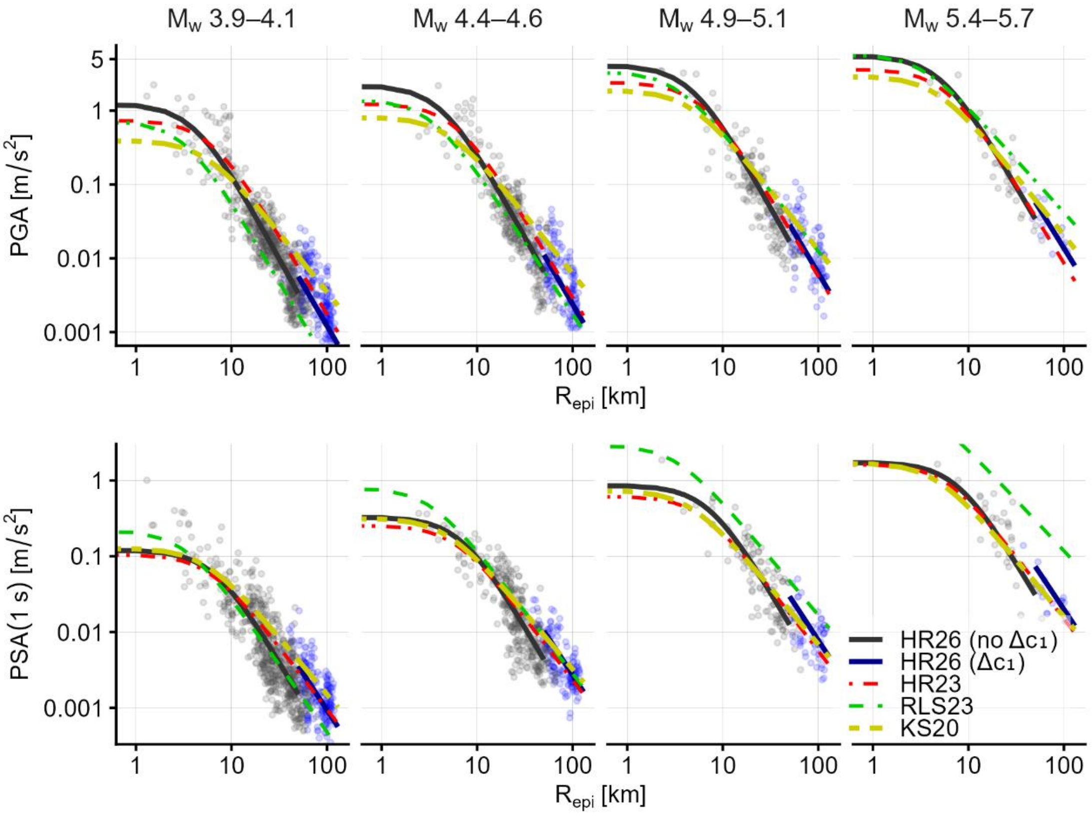

Figure 7. Comparison of observed GMH PGAs (upper panel) and PSAs (1s) (lower panel) recorded by the IceSMN network with the proposed median GMM (HR26) for site class B. For $R_{epi} \geq 45$ km the coefficient $\boldsymbol{\Delta c_1}$ is included. Predictions from HR23 (Hernández-Aguirre et al., 2023), RLS23 (Ramadan et al., 2023), and KS20 (Kowsari et al., 2020) are included for comparison. Records from the South Iceland Lowland path group are indicated by blue markers, whereas all other records are shown in grey.

5.1.2 Residuals and variance components

We evaluate model adequacy by decomposing residuals into between-event terms, station terms, and remaining within-event residuals (Figure 8). The event terms are centred near zero and show no systematic dependence on magnitude, suggesting that the fixed-effects magnitude scaling captures the average source-size dependence over the magnitude range represented in the dataset. The larger spread of event terms at low magnitudes supports the adopted heteroskedastic formulation, with larger between-event variability for small events (τ_1; $M_w \leq 3.5$) transitioning to τ_2 by $M_w \geq 4.5$.

Station terms provide a useful diagnostic of the site model. Posterior station effects are broadly centred around zero with limited remaining systematic structure, consistent with the geology-based site classes capturing first-order site-response trends. Nevertheless, non-negligible station-to-station variability persists, which is expected given that four broad classes cannot fully represent local amplification in southwest Iceland. Shallow lava–soil layering, variable sediment thickness, impedance contrasts, topographic effects, and small-scale volcanic heterogeneity may all contribute the remaining variability.

The remaining within-event residuals exhibit no clear drift with distance, suggesting that the attenuation model provides an adequate description of average propagation effects once event and station terms are removed. In particular, absence of a clear distance-dependent bias indicates that the additional path correction Δc_1 effectively reduces regional path-related residual structure.

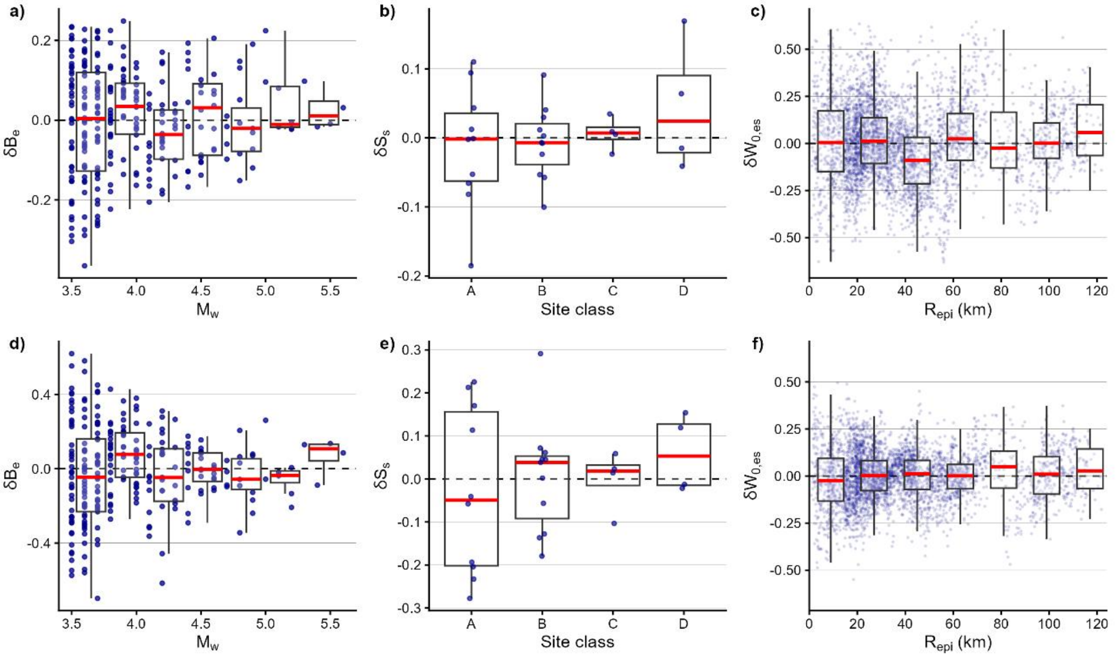

Figure 8. Residual diagnostics for two GMH intensity measures: PGA in the upper row and PSA at T =1 s in the lower row. (**a,d**) Posterior median between-event terms, δB_e, as a function of moment magnitude, M_w. (**b,e**) Posterior median station-to-station terms, δS_s, grouped by site class. (**c,f**) Remaining within-event residuals, $\delta W_{0,es}$, versus R_{epi} after removing the fixed effects, event terms, and station terms. Boxplots summarize distributions within magnitude, site-class, and distance bins; medians are shown in red.

The posterior median standard deviations of the variance components are reported in Table A4 for the horizontal and the vertical models, and their period dependence is summarized in Figure 9. The horizontal and vertical models exhibit broadly similar levels and trends of variability across periods. Among the decomposed components, the station-to-station term contributes the least, whereas the dominant source of variability shifts with period: at short periods the total scatter is largely controlled by the remaining within-event (aleatory) term, while at longer periods the between-event component becomes increasingly important. For the horizontal model, the resulting total standard deviation is lower than that reported by HR23 and values typically reported for volcanic-region GMMs (Ramadan et al., 2023; Scala et al., 2026). This reduction may partly reflect improved median predictions enabled by the additional deep-events term, path terms and the inclusion of site classes.

The between-event variability is larger at low magnitudes (τ_1) than at higher magnitudes (τ_2), consistent with greater event-to-event scatter for small events in Figure 8. The separation between τ_1 and τ_2 becomes more pronounced toward longer periods, indicating increased sensitivity of long-period motion to event-level source characteristics (e.g., stress drop, mechanism variability, and magnitude uncertainty). The smaller τ_2 may partly reflect reduced uncertainty in magnitude and location estimates for larger events, although other sources of event-to-event variability are also likely to contribute.

Overall, the residual diagnostics and variance decomposition indicate that the horizontal model does not exhibit strong systematic bias with respect to magnitude or distance. The remaining variability broadly consistent with the heterogeneous source, path, and site conditions in southwest Iceland.

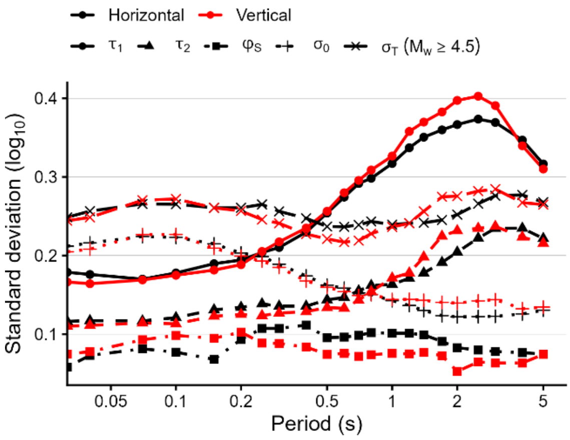

Figure 9. Period dependence of the posterior median standard deviations of the variance components for the GMH (black lines) and the vertical (red lines) models. The total variability (σ_T) is computed for magnitudes larger than 4.5 (i.e., computed with τ_2). Values are shown in log $_{10}$ units.

5.2 Vertical ground-motion

The vertical-component model is one of the principal extensions of this study. HR23 showed that vertical PGA could be comparable to horizontal PGA at several near-source stations, even though vertical PGV was generally lower. This indicates that the vertical component is richer in high-frequency content. The expanded dataset allows this behaviour to be quantified systematically through an independently calibrated vertical GMM. Consequently, the implied vertical-to-horizontal V/H ratio—computed as the ratio of the vertical and horizontal median predictions—is allowed to vary with magnitude, distance, site class, and period, rather than relying of generic V/H relationships derived from global tectonic databases or other volcanic regions. Posterior median fixed-effect coefficients for the vertical IMs are provided in Table A3.

Vertical site-class adjustments are generally smaller than the corresponding horizontal terms, consistent with differences in wavefield composition and near-surface impedance effects that influence vertical amplification. In addition, the estimated path-correction coefficient Δc_1 is markedly smaller than in the horizontal model, suggesting weaker evidence for a systematic Peninsula–South Lowland path contrast in the vertical component within the available dataset.

Figure 10 compares observed vertical PGA and PSA at T = 1 s against the proposed median vertical GMM for site class B. The model reproduces the main distance and magnitude trends and is broadly consistent with the observations. The RLS23 model yields comparable predictions within the magnitude range where it is well constrained (approximately $M_w < 4.6$), although it tends to predict somewhat lower PGA values.

Although median vertical amplitudes are generally lower than horizontal amplitudes (Figure 11a-b), approximately 20% of records with $M_w \geq 4.2$ and $R_{epi} \leq 40$ km exhibit a PGA V/H >1, with maximum observed value approaching 3 (Figure 11c). These observations indicate that vertical demands may be non-negligible for infrastructure located close to active volcanic systems. Similar large V/H ratios have been documented in Italy for both crustal and volcanic earthquakes (Ramadan et al., 2021, 2023; Scala et al., 2026). V/H is highest at short periods (T < 0.15 s), where vertical motion can be comparable to the horizontal component, whereas at longer periods the horizontal spectra dominate (Figure 11b). This behaviour is consistent with HR23, which found lower vertical velocity amplitudes (long-period dominated) and shorter predominant periods for the vertical component.

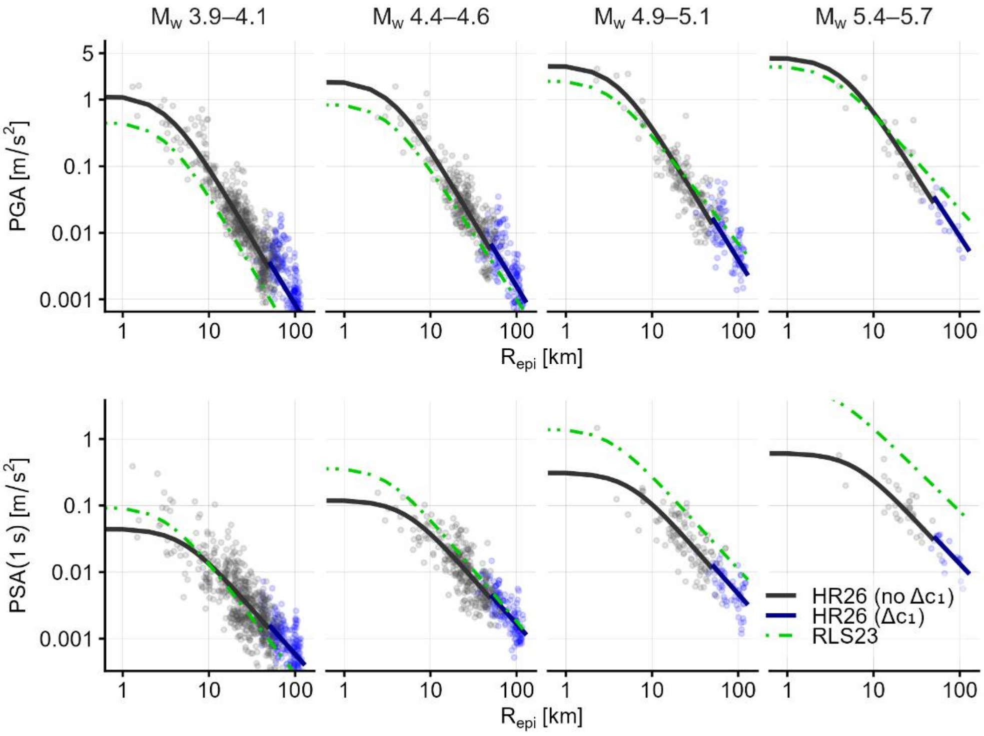

Figure 10. Same as Figure 7 but for the vertical ground-motion model.

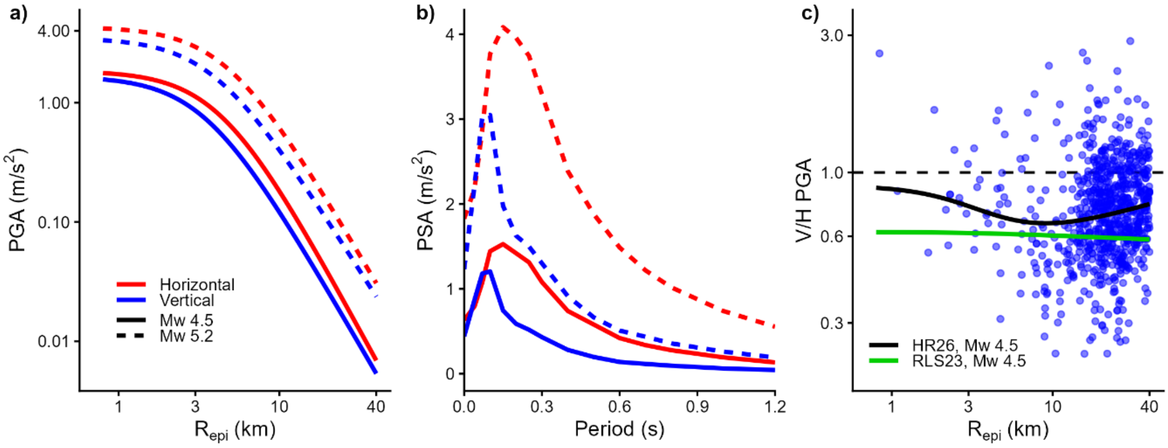

Figure 11. **a)** Comparison between horizontal (red curves) and vertical (blue curves) median PGA against distance for events with M_w = 4.5 (solid lines) and 5.2 (dashed lines). **b)** Comparison between predicted median PSA at R_{epi} = 5km as a function of period for the same cases in a. **c)** V/H ratio from recorded PGA considering events with $M_w \geq 4.2$ and from the median GMMs. All curves correspond to site class B.

6. Discussion and conclusions

This study presents an updated Bayesian ground-motion model (GMM) for volcano-tectonic earthquakes in southwest Iceland. The model extends the first Reykjanes volcano-tectonic GMM of Hernández-Aguirre et al. (2023) by (i) leveraging a substantially expanded strong-motion dataset, (ii) introducing geology-based site classes, (iii) adopting a hierarchical Bayesian mixed-effects formulation, and (iv) providing internally consistent models for both horizontal and vertical spectral accelerations. The final database comprises 4238 records from 273 earthquakes ($M_w \geq 3.5$) at epicentral distances $R_{epi} \leq 120$ km, recorded by the Icelandic Strong Motion Network during the Reykjanes unrest. Developing a dedicated volcano-tectonic GMM is not merely an academic exercise: swarms can occur close to populated areas and lifeline systems, and the recent Fagradalsfjall unrest demonstrated that multiple $M_w \gtrsim 5$ earthquakes may occur within short time windows. Because the updated model predicts relatively strong near-source shaking coupled with rapid attenuation, it is particularly relevant for localized hazard in the Reykjanes Peninsula and portions of the capital region that may be impacted by future episodes of unrest. More broadly, critical infrastructure in volcanic environments—including hydropower facilities and transmission corridors—may be exposed to earthquakes whose scaling differs from the assumptions embedded in tectonic-only hazard models.

6.1 Key findings and implications

The expanded dataset confirms that Reykjanes volcano-tectonic ground motions differ systematically from ordinary tectonic ground motions in Iceland. As in HR23, near-source amplitudes are relatively large and attenuation with distance is faster than in many tectonic GMMs. The persistence of these features after adding an order of magnitude more records and a broader set of stations indicates that they are robust characteristics of the Reykjanes volcano-tectonic regime rather than artefacts of limited sampling. Consequently, applying tectonic models to volcanic settings in southwest Iceland can bias hazard estimates, particularly at sites close to active fissure swarms where short-distance motions dominate engineering demand.

For PSHA, rapid attenuation implies a reduced regional footprint of moderate volcano-tectonic earthquakes compared with more slowly attenuating models, whereas the elevated near-source amplitudes increase hazard locally close to swarm sources. This combination implies that hazard during unrest can be strongly localized: communities and infrastructure in close proximity to active segments (e.g., Grindavík–Svartsengi and nearby corridors) may experience damaging shaking during moderate events, while more distant sites may be less affected than suggested by tectonic-only models. The updated GMM therefore supports a more realistic spatial contrast in hazard for volcanic regions, which is important for both long-term hazard mapping and near-term risk management.

Volcanic swarms can generate multiple moderate earthquakes within days to weeks, as observed during the Fagradalsfjall episodes. Even when individual events remain below Iceland's largest tectonic magnitudes, repeated shaking can affect non-structural components, slopes, pipelines, industrial systems, and public perception of risk. Scenario calculations based on the proposed GMM can therefore inform emergency planning by quantifying expected shaking for plausible swarm locations and magnitudes, and by supporting rapid assessments as unrest migrates spatially.

Introducing geology-based site classes improves both model interpretability and operational use. Site classes B–D generally exhibit increasing short-period amplification relative to class A, consistent with the prevalence of shallow lava–soil layering and variable sediment cover in southwest Iceland. Station random effects capture repeatable deviations not explained by the coarse classification, reducing the tendency for site amplification to alias into magnitude or distance terms. At intermediate-to-long periods, coefficients for classes B and C approach zero, consistent with amplification being controlled primarily by shallow, high-contrast near-surface layering that preferentially affects short-period motions and has limited influence on longer-period response.

The hierarchical Bayesian formulation provides a practical and transparent framework for unbalanced strong-motion datasets typical of volcanic regions, where station coverage and distance sampling can be highly uneven. The model decomposes variability into between-event, station-to-station, and remaining within-event components, and INLA enables efficient posterior inference for fixed effects and variance parameters. Informative priors and the adopted two-step calibration reduce unrealistic trade-offs—particularly between distance scaling and station terms—and stabilize coefficients that are weakly identified at certain periods or in sparse regions of predictor space. This workflow is transferable to other regions where sparse or uneven strong-motion data necessitate physically motivated regularization.

Despite the much larger dataset relative to HR23, the total standard deviation is reduced. The reduction is consistent with improved median fit enabled by the additional predictor terms (e.g., depth/path adjustments) and the inclusion of site classes, which remove systematic structure that would otherwise remain in the residuals. Moreover, the larger dataset improves the stability of median scaling and the partitioning of residual components.

A central extension of this work is the explicit calibration of a vertical GMM. The vertical component exhibits distinct scaling and should not be represented solely through fixed V/H ratios. Near-source vertical PGA can be comparable to horizontal PGA at short periods, which is relevant for components and systems sensitive to vertical acceleration (e.g., short-span elements, cantilevers, industrial equipment, and anchorage-controlled non-structural components). By calibrating vertical and horizontal models independently, the implied V/H ratio becomes a function of magnitude, distance, site class, and period, providing a rational basis for evaluating vertical seismic demand during unrest in Icelandic volcanic areas without relying on ratios imported from global tectonic databases or other volcanic regions.

6.2 Limitations and future work

The proposed model is subject to several limitations. Because the calibration is dominated by earthquakes from the Reykjanes unrest, it should not be assumed representative of all Icelandic volcanic systems, which may differ in mechanisms, depths and attenuation properties; applications outside southwest Iceland should therefore be treated cautiously until additional regional datasets are incorporated. Although the database is substantially larger than in HR23, events above M_w 5 remain relatively few, and extrapolation to larger magnitudes should be avoided without additional constraints; physics-based simulations and/or regionally informed priors provide a practical route to constrain such extrapolations where needed. Epicentral distance is consistently available but imperfect: R_{epi} is generally adequate for small shallow events, whereas rupture-based metrics (e.g., R_{JB} or R_{rup}) are preferable for larger events, but require rupture geometry that is unavailable for most earthquakes; the inclusion of a pseudo-depth partially compensates for finite-source saturation but does not replace explicit finite-fault characterization. The geology-based site classification is a practical proxy for site response, but Icelandic site response is controlled by complex volcanic and sedimentary structure; future work should integrate H/V ratios, site investigation topographic proxies, and empirical site residuals into more detailed site models. Finally, the model is fitted period-by-period, with priors for period i anchored to the posterior from period i-1; however, the model is not jointly estimated across periods and does not include explicit inter-period or inter-component residual correlation, which is needed for conditional spectra and vector-valued hazard.

6.3 Concluding remarks

Taken together, the results support the use of a dedicated volcano-tectonic GMM for southwest Iceland and highlight the limitations of relying on tectonic-only models for volcanic settings. The updated model provides an operational basis for both long-term PSHA and time-dependent scenario assessment during unrest, improves physical interpretability through geology-based site terms, and delivers a regionally calibrated vertical component model that is particularly relevant for near-source short-period demand. Continued updates as new recordings accumulate, together with extensions to residual correlation structure and refined site characterization, will further improve the model’s utility for hazard and risk applications in Icelandic volcanic regions.

The comparison with recent Italian volcanic GMMs is particularly noteworthy. Despite differences in tectonic setting, crustal structure, and volcanic processes, the models show broadly similar behaviour within the magnitude range constrained by both datasets. This suggests that some features of volcano-tectonic ground-motion scaling may be common across volcanic regions, while others remain strongly regional. Expanding such comparisons to additional volcanic environments and developing joint multi-region datasets may provide a pathway toward identifying which aspects of volcanic ground-motion behaviour are universal and which require region-specific calibration.

CRediT authorship contribution statement

VM Hernández-Aguirre: Writing – original draft, Conceptualization, Methodology, Formal analysis. **Rajesh Rupakhety:** Writing – review & editing, Conceptualization, Supervision, Funding acquisition, Resources.

Declaration of competing interest

The authors declare that they have no known competing financial interests or personal relationships that could have appeared to influence the work reported in this paper.

Data availability

Data are available under reasonable request.

Acknowledgements

We are grateful to Símon Ólafsson for his work in maintaining the IceSMN network. We thank Guðný E. Birgisdóttir for performing the moment-tensor inversions and providing the corresponding magnitude estimates used in this study.

Appendix 1. Bayesian GMM parameters

Table A1. Posterior median model parameter values for all GMH IMs.

IM	a	Δa	b_1	b_2	c_1	c_2	Δc_1	s_B	s_C	s_D	h_1
PGA	2.0294	0.019	0.5880	0.3326	-2.3681	0.2568	0.135	0.109	0.275	0.427	4.035
PSA(0.04 s)	1.8817	0.030	0.5500	0.3353	-2.1947	0.2513	0.066	0.105	0.290	0.454	3.136
PSA(0.07 s)	1.9748	0.028	0.5356	0.3255	-2.1653	0.2470	0.057	0.114	0.324	0.479	3.151
PSA(0.1 s)	2.2641	0.023	0.5501	0.3480	-2.3356	0.2095	0.107	0.143	0.363	0.453	3.800
PSA(0.15 s)	2.3534	0.024	0.5831	0.3666	-2.3646	0.1911	0.132	0.139	0.244	0.375	4.061
PSA(0.2 s)	2.5407	0.007	0.6332	0.3667	-2.4738	0.1767	0.179	0.103	0.184	0.399	4.730
PSA(0.25 s)	2.4983	-0.008	0.6643	0.3895	-2.4728	0.1618	0.223	0.100	0.174	0.356	4.556
PSA(0.3 s)	2.3586	-0.022	0.6912	0.4095	-2.4054	0.1803	0.229	0.098	0.183	0.283	4.359
PSA(0.4 s)	2.2241	-0.057	0.7352	0.4040	-2.3495	0.1826	0.229	0.074	0.157	0.216	4.636
PSA(0.5 s)	2.2370	-0.094	0.7799	0.4339	-2.3835	0.1334	0.246	0.064	0.086	0.211	5.372
PSA(0.6 s)	2.1946	-0.107	0.8136	0.4775	-2.3829	0.1473	0.259	0.057	0.022	0.233	6.020
PSA(0.7 s)	2.1814	-0.136	0.8443	0.5296	-2.3937	0.1165	0.269	0.044	-0.016	0.265	6.591
PSA(0.8 s)	2.0180	-0.152	0.8731	0.5819	-2.3040	0.0863	0.255	0.038	-0.030	0.281	6.577
PSA(1 s)	1.7337	-0.196	0.9205	0.6083	-2.1664	0.0657	0.220	0.052	-0.022	0.246	6.579
PSA(1.2 s)	1.3186	-0.222	0.9508	0.6177	-1.9400	0.0923	0.173	0.051	-0.029	0.181	5.690
PSA(1.4 s)	0.9465	-0.244	0.9763	0.6396	-1.7346	0.0715	0.127	0.041	-0.013	0.131	4.844
PSA(1.7 s)	0.6591	-0.267	1.0018	0.6416	-1.6026	0.0996	0.095	0.031	-0.005	0.124	4.355
PSA(2 s)	0.4552	-0.272	1.0318	0.6384	-1.5164	0.1485	0.084	0.015	-0.006	0.101	4.235
PSA(2.5 s)	0.1273	-0.319	1.0514	0.6593	-1.3757	0.1318	0.035	0.007	-0.001	0.062	3.559
PSA(3 s)	-0.1780	-0.338	1.0706	0.6547	-1.2329	0.2129	0.027	0.015	0.013	0.057	2.864
PSA(4 s)	-0.6016	-0.306	1.0721	0.6501	-1.1017	0.4012	0.057	0.027	0.039	0.050	2.079
PSA(5 s)	-0.8819	-0.255	1.0428	0.6487	-1.0920	0.4763	0.076	0.039	0.035	0.069	1.694
PGV	0.8306	-0.078	0.7774	0.3060	-2.3124	0.4484	0.206	0.086	0.129	0.280	4.369

Table A2. Posterior median model parameter values for all RotInv IMs.

IM	a	Δa	b_1	b_2	c_1	c_2	Δc_1	s_B	s_C	s_D	h_1
PGA	2.0538	0.024	0.5901	0.3340	-2.3761	0.2495	0.134	0.116	0.278	0.437	4.017
PSA(0.04 s)	1.9070	0.032	0.5509	0.3381	-2.2035	0.2419	0.066	0.111	0.290	0.461	3.132
PSA(0.07 s)	2.0112	0.032	0.5349	0.3283	-2.1832	0.2383	0.057	0.119	0.334	0.486	3.203
PSA(0.1 s)	2.2797	0.027	0.5468	0.3507	-2.3405	0.2181	0.108	0.146	0.370	0.454	3.742
PSA(0.15 s)	2.3384	0.029	0.5833	0.3655	-2.3431	0.1922	0.122	0.144	0.242	0.380	3.885
PSA(0.2 s)	2.4793	0.012	0.6308	0.3641	-2.4229	0.1920	0.162	0.112	0.185	0.407	4.454
PSA(0.25 s)	2.4573	-0.003	0.6611	0.3809	-2.4337	0.1688	0.213	0.103	0.169	0.360	4.324
PSA(0.3 s)	2.3446	-0.020	0.6923	0.3956	-2.3820	0.1855	0.223	0.098	0.179	0.289	4.157
PSA(0.4 s)	2.2419	-0.055	0.7351	0.3977	-2.3488	0.1851	0.229	0.069	0.155	0.229	4.504
PSA(0.5 s)	2.2660	-0.089	0.7811	0.4340	-2.3921	0.1281	0.247	0.062	0.086	0.224	5.332
PSA(0.6 s)	2.2299	-0.107	0.8174	0.4918	-2.3930	0.1168	0.261	0.056	0.022	0.241	5.998
PSA(0.7 s)	2.2383	-0.137	0.8450	0.5448	-2.4192	0.0968	0.273	0.041	-0.019	0.281	6.612
PSA(0.8 s)	2.0627	-0.153	0.8750	0.5959	-2.3222	0.0764	0.260	0.035	-0.028	0.302	6.560
PSA(1 s)	1.7742	-0.196	0.9214	0.6290	-2.1819	0.0465	0.225	0.053	-0.020	0.262	6.598

PSA(1.2 s)	1.3524	-0.217	0.9520	0.6493	-1.9505	0.0596	0.176	0.051	-0.028	0.191	5.653
PSA(1.4 s)	0.9570	-0.238	0.9777	0.6576	-1.7307	0.0743	0.127	0.040	-0.006	0.145	4.712
PSA(1.7 s)	0.6773	-0.264	1.0010	0.6616	-1.6038	0.0982	0.094	0.030	0.001	0.142	4.230
PSA(2 s)	0.4642	-0.263	1.0307	0.6522	-1.5139	0.1704	0.092	0.016	-0.004	0.111	4.059
PSA(2.5 s)	0.1667	-0.317	1.0499	0.6551	-1.3893	0.1693	0.042	0.006	-0.001	0.064	3.559
PSA(3 s)	-0.1386	-0.340	1.0748	0.6498	-1.2370	0.2231	0.027	0.008	0.012	0.056	2.878
PSA(4 s)	-0.5670	-0.310	1.0817	0.6382	-1.0977	0.4283	0.059	0.018	0.041	0.058	2.048
PSA(5 s)	-0.8438	-0.257	1.0555	0.6283	-1.0919	0.5505	0.094	0.032	0.046	0.078	1.578
PGV	0.8661	-0.075	0.7762	0.3417	-2.3287	0.4441	0.210	0.088	0.127	0.293	4.323

Table A3. Posterior median model parameter values for all vertical IMs.

IM	a	Δa	b_1	b_2	c_1	c_2	Δc_1	s_B	s_C	s_D	h_1
PGA	1.6204	0.051	0.5428	0.3304	-2.1952	0.2745	0.057	0.121	0.178	0.429	3.176
PSA(0.04 s)	1.9121	0.061	0.5054	0.3374	-2.2587	0.2377	0.052	0.100	0.244	0.507	2.735
PSA(0.07 s)	1.8298	0.066	0.5162	0.3457	-2.1235	0.2261	-0.005	0.190	0.268	0.523	2.477
PSA(0.1 s)	1.8646	0.047	0.5389	0.3910	-2.1006	0.1750	0.016	0.152	0.159	0.427	2.634
PSA(0.15 s)	1.6268	0.031	0.5692	0.4024	-1.9773	0.1766	0.038	0.096	0.132	0.390	2.536
PSA(0.2 s)	1.5223	0.005	0.6101	0.4061	-1.9087	0.1679	0.048	0.070	0.109	0.307	2.639
PSA(0.25 s)	1.5327	-0.023	0.6461	0.4046	-1.9417	0.1726	0.070	0.079	0.070	0.247	3.014
PSA(0.3 s)	1.5242	-0.044	0.6753	0.4095	-1.9619	0.1765	0.079	0.075	0.065	0.212	3.438
PSA(0.4 s)	1.3586	-0.085	0.7315	0.3818	-1.8893	0.1884	0.062	0.073	0.027	0.188	3.948
PSA(0.5 s)	1.2206	-0.104	0.7736	0.4128	-1.8248	0.1601	0.034	0.061	0.004	0.179	4.514
PSA(0.6 s)	1.0628	-0.111	0.7964	0.4414	-1.7551	0.1898	0.034	0.039	0.000	0.167	4.617
PSA(0.7 s)	0.9414	-0.131	0.8307	0.4930	-1.6850	0.1597	0.022	0.039	-0.002	0.149	4.776
PSA(0.8 s)	0.7971	-0.167	0.8646	0.5319	-1.6004	0.1175	0.027	0.025	-0.005	0.134	4.803
PSA(1 s)	0.5683	-0.234	0.9064	0.5112	-1.4873	0.1559	0.032	0.017	0.016	0.118	4.805
PSA(1.2 s)	0.2834	-0.273	0.9518	0.5337	-1.2987	0.1326	0.001	-0.006	-0.009	0.068	4.653
PSA(1.4 s)	0.0567	-0.310	0.9920	0.5263	-1.1574	0.1832	-0.013	-0.020	-0.020	0.048	4.378
PSA(1.7 s)	-0.1580	-0.342	1.0281	0.5358	-1.0645	0.1787	-0.001	-0.026	-0.003	-0.025	3.805
PSA(2 s)	-0.3467	-0.367	1.0411	0.5635	-0.9848	0.1552	-0.044	-0.029	-0.025	-0.051	3.132
PSA(2.5 s)	-0.5882	-0.393	1.0716	0.6041	-0.8803	0.0553	-0.108	-0.014	-0.072	0.015	3.024
PSA(3 s)	-0.8185	-0.365	1.0815	0.6313	-0.8281	0.0925	-0.071	0.011	-0.078	0.048	2.400
PSA(4 s)	-1.2467	-0.296	1.0485	0.6559	-0.8094	0.2871	0.037	0.051	-0.051	0.083	1.068
PSA(5 s)	-1.5840	-0.260	0.9934	0.6931	-0.7838	0.3624	0.032	0.067	-0.030	0.089	0.418
PGV	-0.0573	-0.086	0.7542	0.0627	-1.8314	0.6762	0.064	0.074	0.047	0.200	3.352

Table A4. Posterior median standard deviations of variance components (τ_1, τ_2, φ_S, σ_0; $\log_{10}$ units) for each IM and component (GMH, RotInv, and vertical).

IM	GMH				RotDInv				Vertical			
	τ_1	τ_2	φ_S	σ_0	τ_1	τ_2	φ_S	σ_0	τ_1	τ_2	φ_S	σ_0
PGA	0.179	0.116	0.058	0.212	0.179	0.118	0.059	0.216	0.166	0.110	0.075	0.205
PSA(0.04 s)	0.176	0.117	0.073	0.216	0.176	0.118	0.074	0.220	0.164	0.111	0.078	0.208
PSA(0.07 s)	0.170	0.117	0.081	0.224	0.171	0.118	0.082	0.227	0.169	0.114	0.093	0.227
PSA(0.1 s)	0.178	0.121	0.077	0.223	0.178	0.122	0.080	0.226	0.175	0.113	0.098	0.227
PSA(0.15 s)	0.190	0.131	0.068	0.215	0.190	0.132	0.068	0.221	0.182	0.123	0.095	0.209
PSA(0.2 s)	0.194	0.134	0.093	0.203	0.195	0.135	0.091	0.209	0.188	0.125	0.103	0.199
PSA(0.25 s)	0.204	0.139	0.107	0.199	0.207	0.139	0.107	0.203	0.205	0.124	0.089	0.193
PSA(0.3 s)	0.210	0.136	0.107	0.189	0.210	0.137	0.107	0.194	0.217	0.127	0.088	0.185
PSA(0.4 s)	0.230	0.136	0.112	0.174	0.230	0.138	0.112	0.177	0.235	0.129	0.084	0.168
PSA(0.5 s)	0.254	0.144	0.096	0.162	0.253	0.145	0.095	0.167	0.256	0.134	0.074	0.160
PSA(0.6 s)	0.274	0.147	0.096	0.159	0.276	0.147	0.095	0.161	0.280	0.133	0.076	0.154
PSA(0.7 s)	0.292	0.155	0.099	0.153	0.291	0.154	0.098	0.155	0.296	0.143	0.072	0.149
PSA(0.8 s)	0.298	0.162	0.102	0.150	0.298	0.162	0.102	0.154	0.309	0.154	0.074	0.151
PSA(1 s)	0.317	0.163	0.101	0.143	0.318	0.166	0.102	0.147	0.327	0.171	0.076	0.144
PSA(1.2 s)	0.337	0.171	0.101	0.137	0.337	0.173	0.103	0.142	0.358	0.178	0.075	0.144
PSA(1.4 s)	0.351	0.178	0.099	0.130	0.349	0.181	0.101	0.135	0.370	0.198	0.077	0.143
PSA(1.7 s)	0.360	0.191	0.091	0.124	0.361	0.192	0.091	0.127	0.383	0.225	0.073	0.140
PSA(2 s)	0.367	0.204	0.083	0.122	0.368	0.202	0.083	0.127	0.397	0.232	0.053	0.140
PSA(2.5 s)	0.374	0.222	0.080	0.122	0.377	0.222	0.080	0.129	0.403	0.235	0.065	0.142
PSA(3 s)	0.369	0.235	0.078	0.123	0.374	0.235	0.080	0.130	0.391	0.237	0.063	0.144
PSA(4 s)	0.347	0.235	0.077	0.126	0.350	0.236	0.078	0.132	0.340	0.224	0.063	0.132
PSA(5 s)	0.317	0.222	0.075	0.131	0.320	0.228	0.075	0.135	0.310	0.216	0.074	0.135
PGV	0.220	0.133	0.065	0.165	0.219	0.135	0.065	0.168	0.217	0.142	0.052	0.153

References

Arroyo, D., & Ordaz, M. (2010). Multivariate Bayesian Regression Analysis Applied to Ground-Motion Prediction Equations, Part 2: Numerical Example with Actual Data. *Bulletin of the Seismological Society of America*, *100*(4), 1568–1577. https://doi.org/10.1785/0120090320

Bachl, F. E., Lindgren, F., Borchers, D. L., & Illian, J. B. (2019). inlabru: An R package for Bayesian spatial modelling from ecological survey data. *Methods in Ecology and Evolution*, *10*(6), 760–766. https://doi.org/10.1111/2041-210X.13168

Birgisdóttir, G. E. (2025). Seismic Ground Motion and Hazard in the Volcanic Environment: New Insights from the Volcano-Tectonic Unrest in the Reykjanes Peninsula, Iceland. *Master Thesis, University of Iceland, Iceland*.

Björnsson, S., Einarsson, P., Tulinius, H., & Hjartardóttir, Á. R. (2020). Seismicity of the Reykjanes Peninsula 1971–1976. *Journal of Volcanology and Geothermal Research*, *391*, 106369–106369. https://doi.org/10.1016/j.jvolgeores.2018.04.026

Bossu, R., Haslinger, F., & Hébert, H. (2024). History and activities of the European-Mediterranean Seismological Centre. *Seismica*, *3*(1). https://doi.org/10.26443/seismica.v3i1.981

Bouchon, M. (1981). A Simple Method to Calculate Green's Functions for Elastic Layered Media. *Bulletin of the Seismological Society of America*, *71*(4), 959–971.

Darzi, A., Halldorsson, B., Cotton, F., & Rahpeyma, S. (2024). Nationwide Frequency-Dependent Seismic Site Amplification Models for Iceland. *Soil Dynamics and Earthquake Engineering*, *183*. https://doi.org/10.1016/j.soildyn.2024.108798

Ducrocq, C., Árnadóttir, T., Einarsson, P., Jónsson, S., Drouin, V., Geirsson, H., & Hjartardóttir, Á. R. (2024). Widespread fracture movements during a volcano-tectonic unrest: The Reykjanes Peninsula, Iceland, from 2019–2021 TerraSAR-X interferometry. *Bulletin of Volcanology*, *86*(2), 14. https://doi.org/10.1007/s00445-023-01699-0

Einarsson, P. (1991). Earthquakes and Present-Day Tectonism in Iceland. *Tectonophysics*, *189*(1–4), 261–279. https://doi.org/10.1016/0040-1951(91)90501-I

Fischer, T. J., Hrubcová, P., Vlček, J., De Pascale, G. P., Thordarson, T., Geirsson, H., Lomax, A., & Skoumal, R. (2026). Dynamic Coupling Between Faulting, Rifting and Magmatism During 2021-2025 Unrest on Reykjanes Peninsula, Iceland. *Geophysical Research Letters*, *53*(10), e2026GL122058. https://doi.org/10.1029/2026GL122058

Hernández-Aguirre, V. M., Rupakhety, R., Ólafsson, S., Bessason, B., Erlingsson, S., Paolucci, R., & Smerzini, C. (2023). Strong Ground Motion from the Seismic Swarms Preceding the 2021 and 2022 Volcanic Eruptions at Fagradalsfjall, Iceland. *Bulletin of Earthquake Engineering*, *21*(10), 4707–4730. https://doi.org/10.1007/s10518-023-01725-8

Iervolino, I., Cito, P., De Falco, M., Festa, G., Herrmann, M., Lomax, A., Marzocchi, W., Santo, A., Strumia, C., Massaro, L., Scala, A., Scotto Di Uccio, F., & Zollo, A. (2024). Seismic Risk Mitigation at Campi Flegrei in Volcanic Unrest. *Nature Communications*, *15*(1), 10474. https://doi.org/10.1038/s41467-024-55023-1

IMO. (2025). *Earthquake Catalogue*. Icelandic Meteorological Office. https://skjalftalisa.vedur.is/.

Jóhannesson, H., & Sæmundsson, K. (2009). Geological Map of Iceland, 1:600 000, Tectonics. *Icelandic Institute of Natural History*.

Jónasson, K., Bessason, B., Helgadóttir, Á., Einarsson, P., Guðmundsson, G. B., Brandsdóttir, B., Vogfjörd, K. S., & Jónsdóttir, K. (2021). A Harmonised Instrumental Earthquake Catalogue for Iceland and the Northern Mid-Atlantic Ridge. *Natural Hazards and Earth System Sciences*, *21*(7), 2197–2214. https://doi.org/10.5194/nhess-21-2197-2021

Kikuchi, M., & Kanamori, H. (1991). Inversion of complex body waves-III. *Bulletin of the Seismological Society of America*, *81*(6), 2335–2350.

Kowsari, M., Sonnemann, T., Halldorsson, B., Hrafnkelsson, B., Snæbjörnsson, J., & Jónsson, S. (2020). Bayesian Inference of Empirical Ground Motion Models to Pseudo-Spectral Accelerations of South Iceland Seismic Zone Earthquakes Based on Informative Priors. *Soil Dynamics and Earthquake Engineering*, *132*. https://doi.org/10.1016/j.soildyn.2020.106075

Kuehn, N. M. (2021). *A primer for using INLA to estimate ground-motion models*. https://doi.org/https://doi.org/10.31224/osf.io/6ut3p

Kuehn, N. M., & Scherbaum, F. (2015). Ground-motion prediction model building: A multilevel approach. *Bulletin of Earthquake Engineering*, *13*(9), 2481–2491. https://doi.org/10.1007/s10518-015-9732-3

Lanzano, G., & Luzi, L. (2020). A Ground Motion Model for Volcanic Areas in Italy. *Bulletin of Earthquake Engineering*, *18*(1), 57–76. https://doi.org/10.1007/s10518-019-00735-9

Lavrentiadis, G., Abrahamson, N. A., & Kuehn, N. M. (2023). A Non-Ergodic Effective Amplitude Ground-Motion Model for California. *Bulletin of Earthquake Engineering*, *21*(11), 5233–5264. https://doi.org/10.1007/s10518-021-01206-w

Olafsdottir, E. A., Erlingsson, S., & Bessason, B. (2023). Hybrid Non-Invasive Characterization of Soil Strata at Sites with and without Embedded Lava Rock Layers in the South Iceland Seismic Zone. *Bulletin of Engineering Geology and the Environment*, *82*(4). https://doi.org/10.1007/s10064-023-03136-0

Rahpeyma, S., Halldorsson, B., Hrafnkelsson, B., & Darzi, A. (2023). Frequency-Dependent Site Amplification Functions for Key Geological Units in Iceland from a Bayesian Hierarchical Model for Earthquake Strong-Motions. *Soil Dynamics and Earthquake Engineering*, *168*. https://doi.org/10.1016/j.soildyn.2023.107823

Ramadan, F., Lanzano, G., & Sgobba, S. (2023). Vertical Seismic Ground Shaking in the Volcanic Areas of Italy: Prediction Equations and PSHA Examples. *Soil Dynamics and Earthquake Engineering*, *175*, 108228–108228. https://doi.org/10.1016/j.soildyn.2023.108228

Ramadan, F., Smerzini, C., Lanzano, G., & Pacor, F. (2021). An Empirical Model for the Vertical-to-Horizontal Spectral Ratios for Italy. *Earthquake Engineering and Structural Dynamics*, *50*(15), 4121–4141. https://doi.org/10.1002/eqe.3548

Rue, H., Martino, S., & Chopin, N. (2009). Approximate Bayesian Inference for Latent Gaussian models by using Integrated Nested Laplace Approximations. *Journal of the Royal Statistical Society Series B: Statistical Methodology*, *71*(2), 319–392. https://doi.org/10.1111/j.1467-9868.2008.00700.x

Rupakhety, R., & Ólafsson, S. (2015). IceSMN Icelandic Strong Motion Network [Data Set]. *International Federation of Digital Seismograph Networks*. https://doi.org/10.7914/YW8C-NY36

Rupakhety, R., & Sigbjörnsson, R. (2013). Rotation-Invariant Measures of Earthquake Response Spectra. *Bulletin of Earthquake Engineering*, *11*(6), 1885–1893. https://doi.org/10.1007/s10518-013-9472-1

Sæmundsson, K. (1979). *Outline of the geology of Iceland*. *29*, 7–28. https://doi.org/10.33799/jokull1979.29.007

Sæmundsson, K., Sigurgeirsson, M., & Friðleifsson, G. Ó. (2020). Geology and Structure of the Reykjanes Volcanic System, Iceland. *Journal of Volcanology and Geothermal Research*, *391*, 106501–106501. https://doi.org/10.1016/j.jvolgeores.2018.11.022

Scala, A., Strumia, C., Cito, P., Di Uccio, F. S., Festa, G., Iervolino, I., Zollo, A., Bobbio, A., Convertito, V., Elia, L., Emolo, A., & Iaccarino, A. G. (2026). Ground motion models for Campi Flegrei (Italy). *Bulletin of Earthquake Engineering*, *24*(2), 627–655. https://doi.org/10.1007/s10518-025-02315-6

Simpson, D., Håvard, R., Riebler, A., Martins, T. G., & Sørbye, S. H. (2017). Penalising Model Component Complexity: A Principled, Practical Approach to Constructing Priors. *Statistical Science*, *32*(1), 1–28. https://doi.org/10.1214/16-STS576

Sokos, E. N., & Zahradnik, J. (2008). ISOLA a Fortran Code and a Matlab GUI to Perform Multiple-Point Source Inversion of Seismic Data. *Computers and Geosciences*, *34*(8), 967–977. https://doi.org/10.1016/j.cageo.2007.07.005

Stafford, P. J. (2014). Crossed and Nested Mixed-Effects Approaches for Enhanced Model Development and Removal of the Ergodic Assumption in Empirical Ground-Motion Models. *Bulletin of the Seismological Society of America*, *104*(2), 702–719. https://doi.org/10.1785/0120130145

Strasser, F. O., Abrahamson, N. A., & Bommer, J. J. (2009). Sigma: Issues, Insights, and Challenges. *Seismological Research Letters*, *80*(1), 40–56. https://doi.org/10.1785/gssrl.80.1.40

Tusa, G., & Langer, H. (2016). Prediction of Ground Motion Parameters for the Volcanic Area of Mount Etna. *Journal of Seismology*, *20*(1), 1–42. https://doi.org/10.1007/s10950-015-9508-x

Tusa, G., Langer, H., & Azzaro, R. (2020). Localizing Ground-Motion Models in Volcanic Terranes: Shallow Events at Mt. Etna, Italy, Revisited. *Bulletin of the Seismological Society of America*, *110*(6), 2843–2861. https://doi.org/10.1785/0120190325